# Contact Angle of Sessile Drops in Lennard–Jones Systems

Stefan Becker,[†] Herbert M. Urbassek,[‡] Martin Horsch,[*,†] and Hans Hasse[†]

*Laboratory of Engineering Thermodynamics, University of Kaiserslautern, Erwin-Schrödinger-Straße 44, 67663 Kaiserslautern, Germany, and Physics Department and Research Center OPTIMAS, University of Kaiserslautern, Erwin-Schrödinger-Straße 46, 67663 Kaiserslautern, Germany*

E-mail: martin.horsch@mv.uni-kl.de

[*]To whom correspondence should be addressed
[†]Laboratory of Engineering Thermodynamics
[‡]Physics Department and Research Center OPTIMAS

**Abstract**

Molecular dynamics simulations are used for studying the contact angle of nanoscale sessile drops on a planar solid wall in a system interacting via the truncated and shifted Lennard–Jones potential. The entire range between total wetting and dewetting is investigated by varying the solid–fluid dispersive interaction energy. The temperature is varied between the triple point and the critical temperature. A correlation is obtained for the contact angle in dependence of the temperature and the dispersive interaction energy. Size effects are studied by varying the number of fluid particles at otherwise constant conditions, using up to 150000 particles. For particle numbers below 10000, a decrease of the contact angle is found. This is attributed to a dependence of the solid–liquid surface tension on the droplet size. A convergence to a constant contact angle is observed for larger system sizes. The influence of the wall model is studied by varying the density of the wall. The effective solid–fluid dispersive interaction energy at a contact angle of $\theta = 90°$ is found to be independent of temperature and to decrease linearly with the solid density. A correlation is developed which describes the contact angle as a function of the dispersive interaction, the temperature and the solid density. The density profile of the sessile drop and the surrounding vapor phase is described by a correlation combining a sigmoidal function and an oscillation term.

# 1 Introduction

Wetting of a solid phase by a liquid plays an important role in many processes. The equilibrium wetting behavior is often classified by the contact angle $0° \leq \theta \leq 180°$ of a sessile drop. The contact angle depends on the interaction between the particles, namely the fluid–fluid and the solid–fluid interactions. These can be explicitly described with force fields and, hence, the force fields yield the contact angle. While much work is available on force fields which describe the interaction in fluids,[1–13] solid–fluid interactions have been studied less systematically. In that field, mainly adsorption of simple fluids in nanopores is considered[14–20] which enables fitting model parameters to adsorption isotherms. There are also reports on predicting the contact angle with force fields both for droplets,[21–33] and for fluid cylinders.[34,35] However, they are restricted to few particular material combinations such as water on graphene.

The present work is devoted to studying the influence of the dispersive solid–fluid interaction on the contact angle in a model system by molecular dynamics (MD) simulations. This model system consists of a single sessile drop on a planar wall. The truncated and shifted Lennard–Jones (LJTS) potential[36] is used for describing the fluid–fluid, solid–solid as well as the solid–fluid interactions, extending previous studies on interfacial properties of the LJTS fluid.[37–39] The solid–fluid interaction and the temperature are varied and a quantitative correlation describing their influence on the contact angle is presented. The density of the solid substrate affects the total potential of the solid–fluid interaction by the number of interaction sites located in a certain distance to a fluid particle.[40] This is examined in simulations with solids of varying densities. A correlation is established for predicting the contact angle as a function of temperature, solid–fluid dispersive interaction, and solid density. The findings are discussed in the context of the results from different studies on the wetting behavior of Lennard–Jones (LJ) fluids.[18,24–26,30,31,37] Furthermore, an empirical correlation is presented that qualitatively describes the density profile of a sessile drop on a planar wall.

The system sizes accessible to MD simulation are getting closer to the smallest experimental settings, but systematic MD studies like the one carried out in the present study are still limited to

nanoscale scenarios. When dealing with wetting phenomena on the nanoscale, one has to consider effects such as the line tension[41] or a decrease in the liquid–vapor surface tension due to the strong curvature of the interface.[42] In the present study, a brute force approach is used to deal with this: The system size is increased until no dependence of the contact angle on the size is observed. The number of fluid particles finally used is 15000, which is large enough to ensure that a further increase would not lead to significantly different results.

The paper is organized as follows: In section 2, the molecular model and the simulation method are described. The results regarding the size effects, the density profile, the contact angle and the influence of the wall density on the contact angle are presented in section 3 and discussed in section 4. Conclusions are drawn in section 5. Additional information is presented in the supporting information.

# 2 Model and Simulation Method

## 2.1 Molecular Model

Like the original LJ potential $u^{\mathrm{LJ}}(r_{ij}) = 4\,\epsilon[\left(\sigma/r_{ij}\right)^{12} - \left(\sigma/r_{ij}\right)^{6}]$ the LJTS potential[36]

$$u^{\mathrm{LJTS}}(r_{ij}) = \begin{cases} u^{\mathrm{LJ}}(r_{ij}) - u^{\mathrm{LJ}}(r_c), & r_{ij} < r_c \\ 0, & r_{ij} \geq r_c \end{cases} \tag{1}$$

with a cutoff radius of $r_c = 2.5\,\sigma$ can accurately reproduce the thermophysical properties of simple nonpolar fluids, especially noble gases and methane.[38] It is used in the present study to describe all the three interaction types, i.e. fluid–fluid, solid–solid and solid–fluid.

The accurate description of solids usually requires the use of multibody potentials that are computationally more expensive.[43] The present study, however, is not concerned with the properties of a solid phase but rather with the influence of the solid–fluid interaction on the fluid, if solely dispersive and repulsive interactions are present. The wall is represented here by particles arranged in a face–centered cubic (fcc) lattice with the (100) surface exposed to the fluid. To maintain the wall in the solid state, the LJ energy parameter of the solid ($s$) is related to that of the fluid ($f$) by $\epsilon_s = 100\,\epsilon_f$ which essentially yields a static lattice. With the size parameter of the solid $\sigma_s$, the lattice constant of the solid phase is $a = 1.55\,\sigma_s$ and the particle density is $\rho_s = 1.07\,\sigma_s^{-3}$. It may be noted that the present choice of the cutoff radius, i.e. $r_c = 2.5\,\sigma_f$, yields practically the same lattice constant as would have been obtained for $r_c \to \infty$, i.e. for the full LJ potential. Unless stated otherwise, the size parameters of the solid and the fluid are the same in the present study, i.e. $\sigma_s = \sigma_f$. For a set of simulations in which the influence of the solid density is studied, the LJ size parameter of the solid $\sigma_s$ is varied. By scaling down $\sigma_s$, the lattice constant of the solid is decreased and, hence, the density is increased: For the size parameters $\sigma_s = 0.80\,\sigma_f$ and $\sigma_s = 0.646\,\sigma_f$, the solid density is $\rho_s = 2.10\,\sigma_f^{-3}$ and $\rho_s = 4.02\,\sigma_f^{-3}$, respectively.

The dispersive and the repulsive interaction between the solid and the fluid phase is also described by the LJTS potential. The LJ size parameter of the unlike interaction between solid and

fluid particles ($sf$) is chosen to be $\sigma_{sf} = \sigma_f$. Note that $\sigma_{sf} = \sigma_f$ even holds in the cases where the size parameter $\sigma_s$ is varied. The LJ energy parameter of the solid–fluid interaction is scaled by

$$\epsilon_{sf} = \zeta \epsilon_f. \tag{2}$$

$\zeta$ is called reduced solid–fluid interaction energy. Its influence on the contact angle is studied systematically.

## 2.2 Simulation Method

MD simulations in the canonical ensemble are carried out with the program *ls1 MarDyn*[44] to obtain the contact angle dependence on the temperature and the reduced solid–fluid interaction energy. Velocity Scaling was applied for temperature control. The parallelization is accomplished by spatial domain decomposition based on a linked cell data structure. Newton's equations of motion are integrated via the Verlet leapfrog algorithm with a time step of $5 \cdot 10^{-4}\ \epsilon_f^{-1/2}\ m^{1/2}\ \sigma_f$.

A sessile drop on a planar solid wall is simulated (see shanpshot in Figure S.1 in the supporting information). The system contains a single drop, i.e. there is no drop on the opposite side of the wall. This corresponds to the stable configuration in the entire regime of partial wetting ($0° < \theta < 180°$).[22] The wall is located in the $(x,z)$–plane, and $y$ represents the distance from the plane in which the centers of the uppermost wall particles lie. Periodic boundary conditions are applied in all directions, leaving a channel for the fluid between the wall and its periodic image. The size of the simulation box is adapted such that for small contact angles the fluid has sufficient space in lateral dimensions. On the other hand, when large contact angles are expected, the spacing of the channel is chosen sufficiently large to avoid a perturbation of the droplet by the periodic image of the wall. The height of the channel exceeds 30 $\sigma_f$ in all cases, which avoids artifacts due to finite size effects[45] related to the channel height. The number of wall particles varies according to the box dimensions. The wall thickness of two and a half crystal unit cells exceeds the cutoff radius of the fluid and thus avoids periodic artefacts, which could be caused by an interaction of fluid

particles on different sides of the wall. The initial configuration of the system consists of a cuboid with liquid density[38] and a surrounding vapor phase, both in contact with the wall. The number of fluid molecules is 15000 except for a series of simulations conducted to investigate size effects, in which this number is varied. The equilibration time is at least 2.5 million time steps, followed by 3.5 million time steps of production.

The sampling of the density profile $\rho(R,y)$ during the simulation is accomplished via binning in a cylindrical coordinate system, in terms of the distance from the wall $y$ and the distance from the symmetry axis of the droplet $R$. In the vicinity of the solid wall, the fluid is affected by strong ordering effects. By choosing a bin size of 0.1 $\sigma_f$ in the direction normal to the wall, these effects are monitored. The liquid-vapor interface is defined by the arithmetic mean density $(\rho' + \rho'')/2$ where $\rho'$ and $\rho''$ are the saturated bulk densities of the LJTS fluid known from previous studies.[38] As will be shown in section 3, the vapor phase is supersaturated so that the density is higher than the corresponding bulk value at saturation. Nevertheless, the bulk values are employed for the definition of the drop boundary because the location of the interface is rather insensitive to the vapor density. A sphere is fitted to the liquid–vapor interface, considering distances to the wall larger than 2 $\sigma_f$ whereas no weighting factors are introduced in the fitting procedure. The region close to the wall is excluded because it shows perturbations due to strong ordering effects. The tangent on this sphere at the intersection with the wall ($y = 0$) is used to determine the contact angle (cf. Figure 1). The mean contact angle is determined from the density profile averaged over the entire production period. The uncertainty is estimated by the standard deviation of contact angles evaluated every 500 000 time steps during the production period.

The interaction of a fluid particle with the wall is the cumulative interaction of that fluid particle with all wall particles.[40] This cumulative potential $u^{\Sigma}$ depends on the density of the wall and the distance of the particle to the wall $y$. As the wall potential is not uniform but periodic it also depends on the lateral position above the wall, given by $x$ and $z$. At a given lateral position $(x,z)$ of the fluid particle, there is a minimum of this cumulative potential $u^{\Sigma}_{min}(x,z)$ with respect to the

distance $y$ from the wall. The average minimum potential

$$-W = \frac{1}{L_x L_z} \int_0^{L_x} \int_0^{L_z} dx\, dz\, u_{min}^{\Sigma}(x,z), \tag{3}$$

where $L_x$ and $L_z$ denote the system size in lateral dimensions, is defined by the average over these minima. For the LJTS potential used in the present study, $W$ depends linearly on $\zeta$ via Eq. (2). While different measures of the solid–fluid interaction are possible,[31,46] in the present study the magnitude of $W$ is employed as a measure, following Grzelak et al.[31] The calculation of the surface of minimal potential is numerically accomplished by setting up a cubic mesh with a spacing of $\Delta x = \Delta z = 0.031\ \sigma_f$ and $\Delta y = 0.01\ \sigma_f$. The average minimum potential of the standard wall investigated in the present study ($\rho_s = 1.07\ \sigma_s^{-3}$) is given by

$$W = 3.08\ \zeta k T_c, \tag{4}$$

where $k$ is the Boltzmann constant and $T_c = 1.078\ \epsilon_f/k$ is the critical temperature of the LJTS fluid.[38] The average minimum potential is given by $W = 4.83\ \zeta k T_c$ for $\rho_s = 2.10\ \sigma_f^{-3}$, and $W = 8.07\ \zeta k T_c$ for $\rho_s = 4.02\ \sigma_f^{-3}$. In the range of the solid density investigated in the present study, the average minimum potential correlates linearly with the solid density $\rho_s$. $W$ is well described by Eq. (5) (cf. supporting information):

$$W(\zeta, \rho_s) = \left[ 1.7 \frac{\rho_s}{\sigma_f^{-3}} + 1.3 \right] \zeta k T_c. \tag{5}$$

On average, the minimum potential is located $0.96\ \sigma_f$ above the topmost wall layer. The topography of the surface of minimal potential along with the local potential values is shown in the supporting information. According to Grzelak et al.,[31] the molecular roughness of the atomistically–resolved wall does not influence the contact angle. As chemical heterogeneities as a second source for contact angle hysteresis[47] are absent, it can be assumed here that no hysteresis occurs. Thus, the results of this study represent the true thermodynamically stable contact angle.

# 3 Simulation Results

## 3.1 Size Effects

To test the influence of the system size on the contact angle and the validity of the present results, simulations with different numbers of fluid particles at otherwise constant conditions are performed. The simulations are carried out for $T = 0.8\ \epsilon_f/k$ and a reduced solid–fluid interaction energy $\zeta$ of 0.35, 0.5 and 0.65, with numbers of fluid particles $N$ = 750, 1500, 45000 and 150000.

The results are shown in Figure 2. It can be seen that above about $N$ = 10000 fluid particles the observed contact angles do not depend significantly on the system size. For the smaller system sizes, smaller contact angles are observed, consistently. The deviation increases with increasing solid–fluid interaction energy. There are several reasons for this deviation which, however, can not be identified seperately from the deviation of the contact angle.[34] As can be seen in Figure 1, there is a layering effect of the fluid density in vicinity to the wall. For small droplets with $N$ = 750 and 1500 particles, the layering affects the liquid density in the entire droplet and there are no bulk liquid properties.[48] found for planar liquid interfaces a significant decrease in the liquid–vapor interfacial tension due to the absence of bulk liquid properties, which is beyond the Tolman correction to the interfacial tension.[42] In addition to the decrease of the liquid–vapor interfacial tension, the solid–liquid interfacial tension is assumed to decrease by the lack of bulk liquid properties. Another contribution affecting the contact angle is due to the growing influence of the three phase contact line with the line tension $\mathcal{L}$ and the curvature $\kappa$. The influence of these effects can be assessed from[41]

$$\cos\theta = \frac{\gamma_{sv} - \gamma_{sl}}{\gamma_{lv}} - \frac{\mathcal{L}\kappa}{\gamma_{lv}}, \tag{6}$$

i.e. an adequately extended version of the Young equation

$$\cos\theta = \frac{\gamma_{sv} - \gamma_{sl}}{\gamma_{lv}}, \tag{7}$$

which both show that a decrease in $\gamma_{lv}$ would lead to a deviation such that the contact angle would

be lower in the range of acute angles but higher for obtuse contact angles (or vice versa, depending on the sign of the line tension). The decrease in $\gamma_s l$ also contibutes to a persistent decrase in the contact angle. The findings of the present study are in line with those of Santiso et al.:[49] They observed a larger contact angle with an increasing droplet size and also a convergence to a constant angle. In their case the contact angle converged at a system size of about $10^5$ fluid particles which is larger than in the present case. This shift towards larger fluid particle numbers is attributed to the slower decay of their interaction potential as compared to the one used here.

## 3.2 Density Profile

For the case of $N = 15000$ fluid particles, the characteristics of the density profile of the fluid phase are studied at different values of the reduced solid–fluid interaction energy and the temperature. Figure 1 shows a typical density profile of the fluid phase. The sessile drop on the planar wall has the shape of a spherical cap (circular in the two dimensional plot) and in the interfacial region, the density decreases radially from the center of the sphere to the vapor phase value. The typical undulations in density due to the presence of the wall perturb the fluid only in a range of about 5 to 8 $\sigma_f$. The essential features of the liquid and the vapor phase are correlated by the empirical ansatz

$$\begin{aligned} \rho(\mathcal{R}, y) &= f(\mathcal{R})g(y), \\ f(\mathcal{R}) &= \frac{1}{2}(\rho' + \rho'') - \frac{1}{2}(\rho' - \rho'')\tanh\left(\frac{2(\mathcal{R} - \mathcal{R}_e)}{D}\right), \\ g(y) &= 1 + A\sin\left(\left(\frac{y}{p} - s\right)2\pi\right)\exp(-cy), \end{aligned} \tag{8}$$

where $f(\mathcal{R})$ is the conventional function describing the density profile of a liquid drop surrounded by its vapor phase,[50] with the liquid and vapor densities $\rho'$ and $\rho''$, respectively. The radius of the drop is $\mathcal{R}_e$ and the interfacial thickness is $D$. Similarly, the sessile drop is considered as having a spherical shape, so that the density varies with radial distance $\mathcal{R}$ from the origin of the sphere. The undulations of the fluid density in vicinity to the wall are modeled by a sinusoidal oscillation term

with an amplitude $A$ and a period $p$. The damping parameter $c$ characterizes the exponential decay of these undulations in terms of the distance from the wall $y$. There are eight parameters $\rho'$, $\rho''$, $\mathcal{R}_e$, $D$, $A$, $p$, $s$ and $c$ that are determined from fitting the correlation (8) for each profile. The numerical values of the parameters are given in the supporting information. Figure 3 shows the correlation in cylindrical coordinates (left) and along the symmetry axis of the droplet (right) for the case of $\zeta = 0.65$ and $T = 0.8\ \epsilon_f/k$. In Figure 3, $R$ denotes the distance from the symmetry axis of the drop, i.e. a cylindrical coordinate, as opposed to the spherical coordinate $\mathcal{R}$ from Eq. (8).

The correlation performs best for intermediate values of the reduced solid–fluid interaction energy for which the contact angle ranges from approximately 45° to 135°. Beyond that range, the correlation shows significant deviations from the densities observed in the simulation. The curvature of the liquid–vapor interface yields vapor densities that differ from the saturation densities in the planar case due to the additional Laplace pressure.[50] The densities that are obtained from Eq. (8) are compared to the saturation densities which are obtained by the conditions of phase equilibrium for curved interfaces. A more detailed description can be found in the supporting information. Fair agreement between the fluid densities obtained via Eq. (8) and the saturation densities for the curved interface is found. The average deviation of the liquid density is 2.2 % and that of the vapor density is 6.9 %. The interfacial thickness $D$ varies between 2.3 $\sigma_f$ at $T = 0.7\ \epsilon_f/k$ and about 8 $\sigma_f$ at $T = 1.0\ \epsilon_f/k$ which agrees with the results of Vrabec et al.[38] The period $p$ of the density undulations is found to be about 0.9 $\sigma_f$ throughout, as it is characteristic for a packing structure. The damping parameter $c$ of the density undulations increases from 0.5 $\sigma_f^{-1}$ to 3.0 $\sigma_f^{-1}$ at elevated temperatures and low values of the reduced solid–fluid interaction energy. It corresponds to a decay length of about 2 $\sigma_f$ at low temperatures and strong interaction to 0.3 $\sigma_f$ at high temperatures and weak interaction, respectively. The radius $\mathcal{R}_e$ of the drop from Eq. (8) agrees well with the dividing surface that is determined by the threshold $\rho = (\rho' + \rho'')/2$. As the interfacial thickness and the density undulations are independent from the system size,[51] the density profile can be extrapolated to droplets of different size.

## 3.3 Contact Angle

The reduced solid–fluid interaction energies are varied at temperatures between 0.7 and 1.0 $\epsilon_f/k$. This covers most of the range of the vapor–liquid coexistence of the LJTS fluid between the triple point[39] at the temperature 0.65 $\epsilon_f/k$ and the critical point[38] at the temperature 1.078 $\epsilon_f/k$. The simulation results are shown in Figure 4 and Figure 5, and the corresponding numerical data are listed in the supporting information.For values of the reduced solid–fluid interaction between 0.25 and 0.75, the contact angle varies from total wetting to total dewetting (i.e. $0° \leq \theta \leq 180°$). The correlation

$$\cos\theta(\tau,\zeta) = \alpha(1+\tau^{\delta})(\zeta-\zeta_0), \tag{9}$$

where $\tau = (1-T/T_c)$, was adjusted to the simulation results and yields good agreement for $\alpha = 1.03$, $\delta = -0.69$, and $\zeta_0 = 0.514$, cf. Figure 4. While it is not fully resolved wheter the nature of the drying transition is first or second order in the case of short range potentials,[24,52] the linear correlation was chosen as it shows only minor differences to the simulation data. The parameter $\delta$ that characterizes the temperature dependence of the contact angle is assumed to be independent from the solid–fluid potential and to solely depend on the temperature. Thus, it is fixed to $\delta = -0.69$ throughout. Due to the linear relation between the average minimum potential and the reduced solid–fluid interaction energy $\zeta$ (Eq. (4)), this transforms to

$$\cos\theta(\tau,W) = \frac{\bar{\alpha}}{kT_c}(1+\tau^{\delta})(W-W_0), \tag{10}$$

with $\bar{\alpha} = 0.335$. The contact angle $\theta = 90°$ occurs at $\zeta_0$ and thus at an average minimum potential given by $W_0 = W(\zeta_0) = 1.58\ kT_c$. The value of $\zeta_0$, and hence that of $W_0$, are both found to be independent of temperature, confirming previous work.[37] High values of $\zeta$ correspond to a strong attraction between the fluid and the wall. As expected, an increasing solid–fluid attraction leads to a decreasing contact angle (see Figure 4).

Eqs. (9) and (10) confirm the symmetry relation

$$\cos\theta(\tau,\zeta_0+\Delta\zeta) = -\cos\theta(\tau,\zeta_0-\Delta\zeta) \tag{11}$$

previously found by Horsch et al.,[37] Sikkenk et al.[22] as well as Monson[53] both by MD simulations and by DFT calculations.

The Young equation,[54] cf. Eq. (7), relates the contact angle $\theta$ to the interfacial tensions $\gamma_{sv}$, $\gamma_{sl}$ and $\gamma_{lv}$ of the solid–vapor, solid–liquid and liquid–vapor interfaces, respectively. The liquid–vapor interfacial tension $\gamma_{lv}$ is not affected by the solid–fluid interaction. At a given temperature, it follows from Eqs. (9) and (7) that the interfacial tension difference $\gamma_{sv}-\gamma_{sl}$ varies linearly with the reduced solid–fluid interaction energy $\zeta$. At $\theta = 90°$ the interfacial tensions $\gamma_{sv}$ and $\gamma_{sl}$ are equal. The present simulation results indicate that the conditions for which $\gamma_{sv} = \gamma_{sl}$ is fulfilled do not depend on the temperature.

The influence of the temperature on the contact angle is shown in Figure 5: The extent of wetting or dewetting increases at elevated temperatures. Applying the Young equation indicates that the ratio of $|\gamma_{sv}-\gamma_{sl}|/\gamma_{lv}$ increases at higher temperatures. A transition occurs when $|\gamma_{sv}-\gamma_{sl}| = \gamma_{lv}$. For the case of a contact angle of 180°, an intrusion of a solid–vapor interface below the droplet is observed, cf. Figure 1 (right).

## 3.4 Wall Density

In order to study the influence of the solid density on the contact angle, simulations are carried out not only for a wall of the density of $\rho_s = 1.07\ \sigma_f^{-3}$ (results discussed above) but also for walls of two other densities: $\rho_s = 2.10\ \sigma_f^{-3}$ and $\rho_s = 4.02\ \sigma_f^{-3}$. The simulation results for the contact angles on surfaces with increased solid densities are correlated by Eq. (10) using the same value for $\delta = -0.69$ as given above, but newly adjusted values for the average minimum potential at $\theta = 90°$, which is given by $W_0$, and the gradient $\bar{\alpha}$. The numerical results are shown in the supporting information. In particular, both $W_0$ and $\bar{\alpha}$ are found to depend linearly on the solid density $\rho_s$. Correlations for

$W_0(\rho_s)$ and $\bar{\alpha}(W_0)$ are obtained by fitting expressions

$$W_0(\rho_s)/kT_c = \eta_1 \frac{\rho_s}{\sigma_f^{-3}} + \eta_2, \tag{12}$$

$$\bar{\alpha}(\rho_s) = \eta_3 \frac{\rho_s}{\sigma_f^{-3}} + \eta_4, \tag{13}$$

to the present simulation results. Good results are obtained for $\eta_1 = 0.36$, $\eta_2 = 1.1$, $\eta_3 = -0.04$, and $\eta_4 = 0.38$ (cf. Figure 6).

# 4 Discussion

Contact angles in LJ systems have been studied by different authors before. Table 1 gives an overview in which also the results of the present study are summarized. There are two additional studies: One by Bucior et al.[18] who have investigated systems with only a single layer of wall interaction sites, arranged in a closest hexagonal packing. In the study of Horsch et al.,[37] the wall model was meant to represent graphite. Both wall models are characterized by a high lateral density. In the case of the graphite model, the interlayer distance is large (about 0.9 $\sigma_f$). The arrangement of the solid sites in both studies was forced, and densities vary significantly from the equilibrium configuration for a solid interacting via a LJ potential. The potential characteristics will therefore be different from those of the other studies. Accordingly, their results are not quantitatively comparable to the other investigations (e.g. see the data of Horsch et al.[37] in Figure S.3 in the supporting information). Therefore, the studies of Bucior et al.[18] and Horsch et al.[37] are not further discussed here. Furthermore, there are studies that basically mimic one of the models discussed here for the purpose of comparison.[32,33] They are not considered in the present discussion, either.

The solid–fluid potential of the literature models differ both in the potential type and the cutoff radius. Ingebrigtsen and Toxvaerd[30] have used a continuous LJ 9–3 potential representing the cumulative interaction of a fluid particle with the wall. Shahraz et al.[35] have also used a contiuous LJ 9–3 potential that differs from the model of Ingebrigtsen and Toxvaerd[30] in the ineraction strength. Furthermore, Shahraz et al.[35] consider a simulation setup where they investigate the contact angle of an infinitely long cylindrical LJ droplet. All other studies mentioned here consider droplets assuming the shape of a spherical cap. Nijmeijer et al.[25] have used a combination of a particulate and continuous LJ 9–3 solid–fluid potential, whereas all other authors[24,26,31] have used particulate models. The solid density was similar for the studies of Ingebrigtsen et al.,[30] Tang and Harris,[26] and Grzelak et al.[31] ($\rho_s \approx 0.6\ \sigma_f^{-3}$). Grzelak et al.[31] have studied the contact angle on several wall models at a constant solid density $\rho_s = 0.58\ \sigma_f^{-3}$, but for various lattice structures and surface orientations. They found a strong correlation between the average minimum potential

and the contact angle, i.e. the contact angle was well characterized by the average minimum potential. For that reason, only one of the wall models of that literature source is discussed in the present study, namely the body centered cubic (bcc) wall with the (100) surface exposed to the fluid. In the following, it is referred to as the "bcc (100) lattice". Furthermore, there are several closely related MD studies on wetting in a LJ system by Sikkenk et al.[21,22] as well as Nijmeijer et al.[23–25] All these studies use very similar molecular models and scenarios. The present discussion exemplarily refers to two of those studies, both by Nijmeijer et al.[24,25] In those simulations, the solid density was $\rho_s = 1.78\ \sigma_f^{-3}$. In the first study,[24] the solid–fluid potential was particulate. The other simulation study discussed here[25] used a particulate solid–fluid potential and an additional cutoff correction in form of a LJ 9–3 potential. This is referred to as the Nijmeijer et al.[25] combined model, in the following. It is similar to the one used by Ingebrigtsen and Toxvaerd[30] and it was meant to account for the long range contribution of the LJ potential. However, while the Nijmeijer et al.[25] combined model does consider a long–range correction contribution to the forces acting on fluid particles at distances $y > r_c$ from the wall, the long–range forces are completely neglected close to the wall ($y \leq r_c$). Thereby, the Nijmeijer et al.[25] combined model, which is considered here nonetheless, fails to consistently address the issue of scale separation, since both short–range and long–range forces are actually strongest close to the wall. The way this combined potential was implemented therefore seems to be inconsistent to the present authors.

The studies of the different authors are carried out at constant but different temperatures. For some of the studies[30,31,35] mentioned above, the average minimum potential $W$ could be directly obtained from the the literature source. For the studies of Nijmeijer et al.[24,25] as well as Tang and Harris,[26] the walls were reconstructed and the average minimum potential was calculated using Eq. (3). It may be noted that for the earlier study of Nijmeijer et al.,[24] the corrected value of the solid–fluid cutoff radius of 2.21 $\sigma_f$ was used, as it was reported in the erratum in the subsequent paper by Nijmeijer et al.[25] The simulation data for the contact angles from the literature were fitted using Eq. (10) with $\delta = -0.69$. The results of the fit for the two correlation parameters $W_0$ and $\bar{\alpha}$, that were adjusted to the literature data, are included in Table 1. They are very well predicted by

the correlation obtained from the simulation data of the present work, cf. Eqs. (12) and (13). The results of the Nijmeijer et al.[25] combined model, however, deviate considerably.

The results from the correlations obtained in the present study can furthermore directly be compared to the simulation data for the contact angle from the different sources. The contact angles are predicted by Eq. (10) using solely the information on the temperature and the solid density given in the literature sources. The solid density was used to determine $\bar{\alpha}(\rho_s)$ and $W_0(\rho_s)$ via Eqs. (12) and (13). The final correlation has the form

$$\cos\theta(\tau, W, \rho_s) = \left(\eta_1 \frac{\rho_s}{\sigma_f^{-3}} + \eta_2\right)\left(1 + \tau^{\delta}\right)\left[W - \left(\eta_3 \frac{\rho_s}{\sigma_f^{-3}} + \eta_4\right)\right], \tag{14}$$

with the parameters $\eta_i$, $i = 1...4$ and $\delta = -0.69$ as introduced above. As can be seen from Figure 7, a good agreement is obtained for most of the simulation data from the literature sources. The results of the Nijmeijer et al.[25] combined model differ considerably from the prediction, which is attributed to the special type of the solid–fluid potential that was mentioned before. Also, the contact angle data of the cylindrical droplet from the study of Shahraz et al.[35] deviate. This might be attributed to the different topology of their simulation setup. The general agreement between Eq. (14) and the simulation data is also obtained for literature data that are not shown in Figure 7, for clarity.

# 5 Conclusions

Sessile drops on a solid wall were studied in a LJTS system. The temperature, the wall density, and the strength of the dispersive fluid–solid interaction were systematically varied. Simulation results for the contact angle as a function of these parameters were obtained. The present simulation data considerably extend the previously available information on systems of the studied type. A correlation which describes the dependence of the contact angle on the parameters mentioned above was developed using the data from the present study. This novel and general correlation agrees well with simulation data obtained by other authors in previous studies on the contact angle in LJ systems, even though details of the models differ.

# 6 Acknowledgement

The authors gratefully acknowledge financial support by the DFG within CRC 926 “Microscale Morphology of Component Surfaces”. Computational support is acknowledged by the Leibniz Supercomputing Center (LRZ) under the large-scale grant pr83ri and the Regional University Computing Center Kaiserslautern (RHRK) under the grant TUKL–MSWS. The authors thank Tobias Alter for carrying out some of the simulations, as well as Cemal Engin and Jadran Vrabec for fruitful discussions. The present work was conducted under the auspices of the Boltzmann–Zuse Society for Computational Molecular Engineering (BZS).

# 7 Tables and Figures

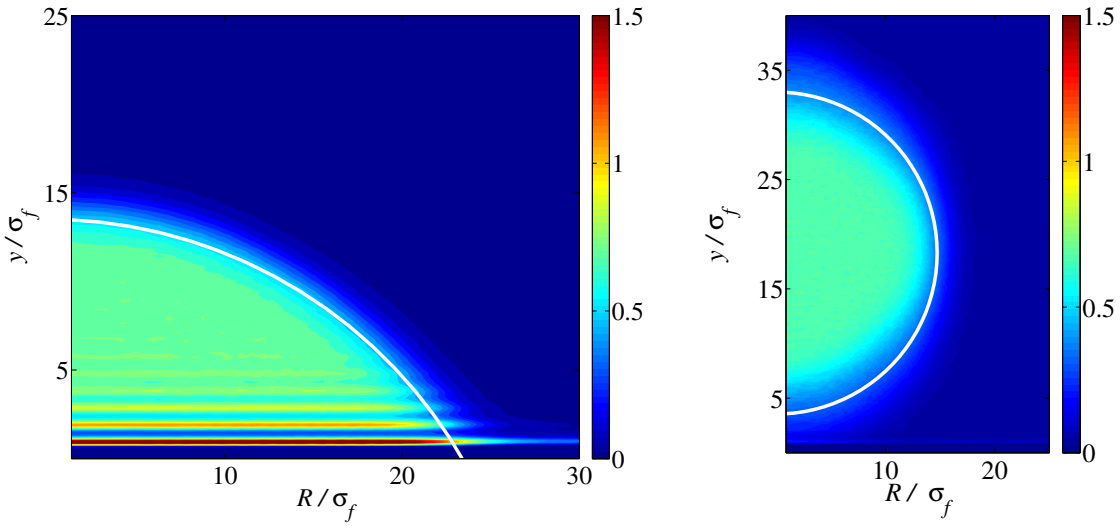


Figure 1: Density profiles of liquid droplets. The color indicates the density in units of $\sigma_f^{-3}$. The white circle is fitted to the interface at the positions with $\rho = (\rho' + \rho'')/2$ and employed to determine the contact angle by extrapolating to $y = 0$. Left: The reduced solid–fluid interaction energy is $\zeta = 0.65$ and the temperature $T = 0.8\ \epsilon_f/k$. An adsorbed fluid phase can be observed next to the droplet. Right: Density profile of a droplet under conditions of total dewetting. The simulation parameters are $\zeta = 0.25$ and $T = 0.9\ \epsilon_f/k$.

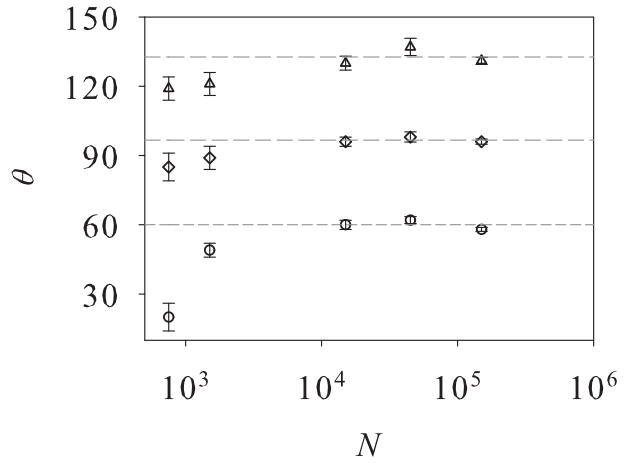


Figure 2: Impact of the number of fluid particles $N$ in the simulation box on the contact angle $\theta$ at $T = 0.8\ \epsilon_f/k$ and reduced solid–fluid interaction energies $\zeta$ of 0.35 (△), 0.5 (◇) and 0.65 (○). The dotted lines correspond to the average of the results for the three largest particle numbers $N$.

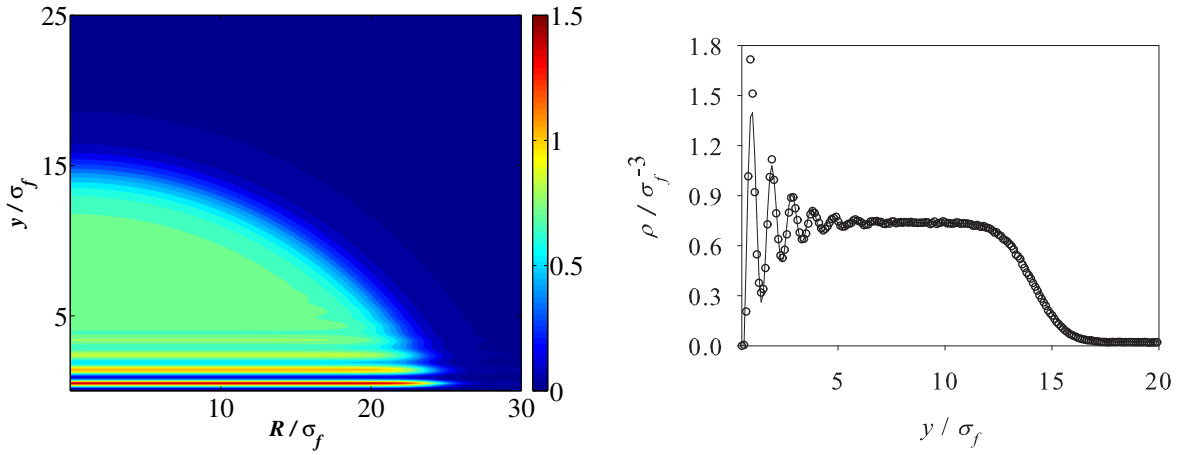


Figure 3: Left: Correlation, cf. Eq. (8), of the density profile of a liquid drop adjusted to the data shown in Figure 1, i.e. for a sessile drop at $\zeta = 0.65$ and $T = 0.8\ \epsilon_f/k$. Left: Two dimensional profile as obtained by the Eq. (8). The color indicates the density in units of $\sigma_f^{-3}$. Right: Simulation results ($\circ$) and correlation (–), cf Eq. (8), for the density profile along the axis of symmetry of the droplet ($R = 0$) over distance from the wall.

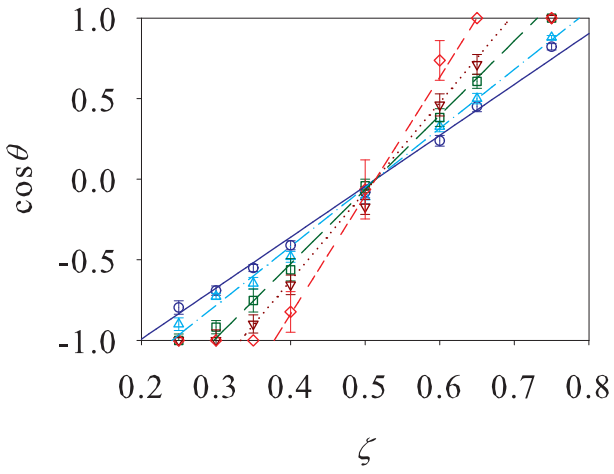


Figure 4: Simulation results (symbols) and correlation (lines), cf. Eq. (9), for the contact angle as a function of the reduced solid–fluid interaction energy at temperatures of $T = 0.7$ ($\circ$, ———), 0.8 ($\triangle$, $-\cdot-\cdot$), 0.9 ($\square$, — — ), 0.95 ($\triangledown$, ·····) and 1.0 $\epsilon_f/k$ ($\diamond$, $---$). The wall density is $\rho_s = 1.07\ \sigma_f^{-3}$, i.e. $\sigma_s = \sigma_f$.

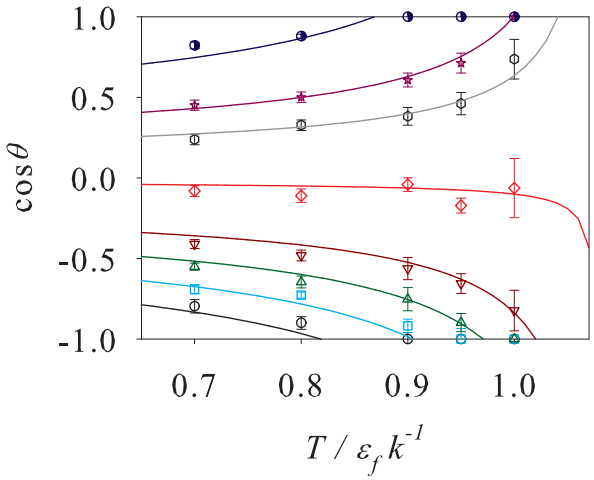


Figure 5: Simulation results (symbols) and correlation (lines), cf. Eq. (9), for the contact angle as a function of temperature at values of the solid–fluid interaction energy $\zeta$ of 0.25 (○), 0.3 (□), 0.35 (△), 0.4 (▽), 0.5 (◇), 0.6 (⬡), 0.65 (☆) and 0.75 (◑). The wall density is $\rho_s = 1.07\ \sigma_f^{-3}$, i.e. $\sigma_s = \sigma_f$.

.

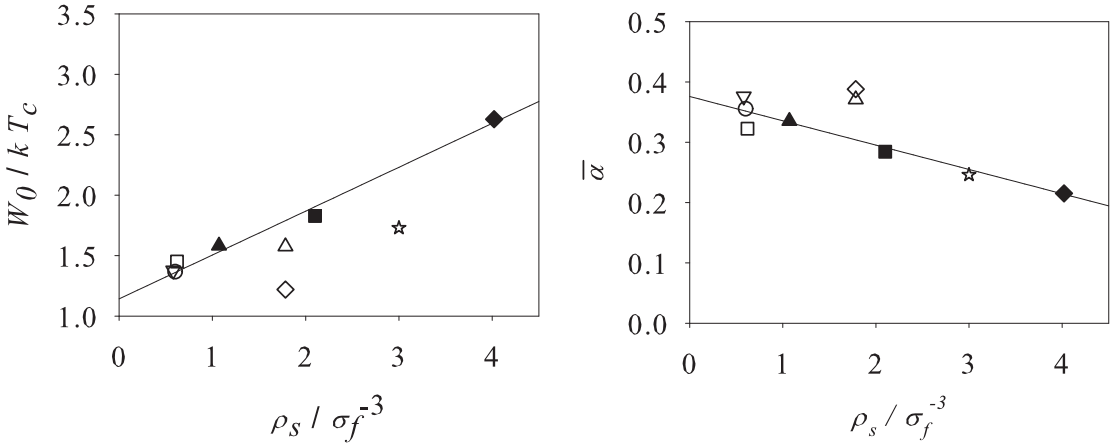


Figure 6: Left: Value of $W_0$, corresponding to the average minimum potential that yields $\theta = 90°$, for wall models of different density. Right: Gradient $\bar{\alpha}$ of the contact angle cosine over the solid density. This work: $\rho_s = 1.07\sigma_f^{-3}$ (▲), $\rho_s = 2.10\sigma_f^{-3}$ (■), $\rho_s = 4.02\sigma_f^{-3}$ (◆). Ingebrigtsen and Toxvaerd[30] (○); Shaharaz et al.[35] (☆); Grzelak et al.,[31] bcc (100) lattice (▽); Tang and Harris[26] (□); Nijmeijer et al.[24] (△); Nijmeijer et al.[25] combined model (◇); The lines represent the fit obtained using from the present simulation data using Eqs. (12) and (13). The parameters are $\eta_1 = 0.36$, $\eta_2 = 1.1$, $\eta_3 = -0.04$, and $\eta_4 = 0.38$.

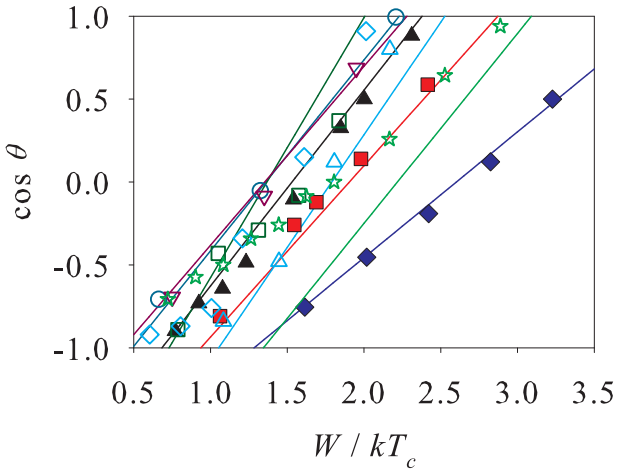


Figure 7: Contact angle cosine over the absolute magnitude $W$ of the average minimum potential. The lines represent Eq. (14) with the parameters $\eta_1 = 0.36$, $\eta_2 = 1.1$, $\eta_3 = -0.04$, and $\eta_4 = 0.38$. The symbols are the simulation results at different temperatures $T$. This work at a temperature of $0.8\epsilon_f/k$: $\rho_s = 1.07\sigma_f^{-3}$ (▲), $\rho_s = 2.10\sigma_f^{-3}$ (■), $\rho_s = 4.02\sigma_f^{-3}$ (◆). Ingebrigtsen and Toxvaerd,[30] 0.75 $\epsilon_f/k$, (○); Shaharaz et al.,[35] 0.7 $\epsilon_f/k$, (☆); Grzelak et al.,[31] bcc (100) lattice, 0.70 $\epsilon_f/k$, (▽); Tang and Harris,[26] 0.90 $\epsilon_f/k$,(□); Nijmeijer et al.,[24] 0.90 $\epsilon_f/k$, (△); Nijmeijer et al.[25] combined model (◇). The simulation results and the corresponding lines representing Eq. (14) are linked by the colors.

Table 1: LJ model systems used for studies on wetting. The solid–fluid potential of Ingebrigtsen and Toxvaerd[30] and of Shaharaz et al.[35] is a continuous LJ 9–3 model, all other potentials are particulate LJ 12–6 models. The values of $W/\zeta$ were obtained from the literature sources (see text). The parameters $W_0$ and $\bar{\alpha}$ of a correlation of the literature data based on Eq. (10) are given.

| source | $\rho_s/\sigma_f^{-3}$ | $r_{c,sf}/\sigma_f$ | $T/\epsilon_f/k$ | $W/\zeta kT_c$ | $W_0/kT_c$ | $\bar{\alpha}$ |
|---|---|---|---|---|---|---|
| Ingebrigtsen and Toxvaerd[30] | 0.60 | ∞ | 0.75 | 1.32 | 1.37 | 0.356 |
| Shaharaz et al.[35] | 3.0 | ∞ | 0.7 | 3.61 | 1.73 | 0.246 |
| Grzelak et al.[31] bcc(100) lattice | 0.58 | 5.00 | 0.70 | 3.00 | 1.38 | 0.376 |
| Tang and Harris[26] | 0.62 | 2.75 | 0.90 | 2.62 | 1.45 | 0.323 |
| Nijmeijer et al.[24] | 1.78 | 2.21 | 0.90 | 3.61 | 1.58 | 0.371 |
| Nijmeijer et al.[25] combined model | 1.78 | 2.35 | 0.90 | 4.03 | 1.22 | 0.338 |
| this work | 1.07 | 2.50 | 0.80 | 3.08 | 1.58 | 0.335 |
| | 2.10 | 2.50 | 0.80 | 4.83 | 1.82 | 0.288 |
| | 4.02 | 2.5 | 0.80 | 8.07 | 2.67 | 0.215 |

## References


(1) Jorgensen, W. L.; Tirado-Rives, J. The OPLS [optimized potentials for liquid simulations] potential functions for proteins, energy minimizations for crystals of cyclic peptides and crambin. *J. Am. Chem. Soc.* **1988**, *110*, 1657–1666.

(2) Jorgensen, W. L.; Maxwell, D. S.; Tirado-Rives, J. Development and Testing of the OPLS All-Atom Force Field on Conformational Energetics and Properties of Organic Liquids. *J. Am. Chem. Soc.* **1996**, *118*, 11225–11236.

(3) Martin, M. G.; Siepmann, J. I. Transferable Potentials for Phase Equilibria. 1. United-Atom Description of n-Alkanes. *J. Phys. Chem. B* **1998**, *102*, 2569–2577.

(4) Keasler, S. J.; Charan, S. M.; Wick, C. D.; Economou, I. G.; Siepmann, J. I. Transferable Potentials for Phase Equilibria–United Atom Description of Five- and Six-Membered Cyclic Alkanes and Ethers. *J. Phys. Chem. B* **2012**, *116*, 11234–11246, PMID: 22900670.

(5) Kiyohara, K.; Gubbins, K.; Panagiotopoulos, A. Phase coexistence properties of polarizable water models. *Mol. Phys.* **1998**, *94*, 803–808.

(6) Potoff, J. J.; Errington, J. R.; Panagiotopoulos, A. Molecular simulation of phase equilibria for mixtures of polar and non-polar components. *Mol. Phys.* **1999**, *97*, 1073–1083.

(7) MacKerell, A. D.; Banavali, N.; Foloppe, N. Development and current status of the CHARMM force field for nucleic acids. *Biopolymers* **2000**, *56*, 257–265.

(8) Vrabec, J.; Stoll, J.; Hasse, H. A Set of Molecular Models for Symmetric Quadrupolar Fluids. *J. Phys. Chem. B* **2001**, *105*, 12126–12133.

(9) Stoll, J.; Vrabec, J.; Hasse, H. Comprehensive study of the vapour-liquid equilibria of the pure two-centre Lennard-Jones plus pointdipole fluid. *Fluid Phase Equilib.* **2003**, *209*, 29–53.

(10) Vorholz, J.; Harismiadis, V.; Panagiotopoulos, A.; Rumpf, B.; Maurer, G. Molecular simulation of the solubility of carbon dioxide in aqueous solutions of sodium chloride. *Fluid Phase Equilib.* **2004**, *226*, 237–250.

(11) Moghaddam, S.; Panagiotopoulos, A. Z. Determination of second virial coefficients by grand canonical Monte Carlo simulations. *Fluid Phase Equilib.* **2004**, *222–223*, 221–224.

(12) Deublein, S.; Vrabec, J.; Hasse, H. A set of molecular models for alkali and halide ions in aqueous solution. *J. Chem. Phys.* **2012**, *136*, 084501.

(13) Merker, T.; Vrabec, J.; Hasse, H. Engineering Molecular Models: Efficient Parameterization Procedure and Cyclohexanol as Case Study. *Soft Mater.* **2012**, *10*, 3–25.

(14) Schapotschnikow, P.; Pool, R.; Vlugt, T. J. H. Selective adsorption of alkyl thiols on gold in different geometries. *Comput. Phys. Commun.* **2007**, *177*, 154–157.

(15) Steele, W. A. *The Interaction of Gases with Solid Surfaces*, 1st ed.; Pergamon: Oxford, 1974.

(16) Findenegg, G. H.; Fischer, J. Adsorption of fluids: simple theories for the density profile in a fluid near an adsorbing surface. *Faraday Discuss. Chem. Soc.* **1975**, *59*, 38–45.

(17) Fischer, J.; Bohn, M.; Körner, B.; Findenegg, G. H. Gasadsorption in Poren. *Chem. Ing. Tech.* **1982**, *54*, 763–763.

(18) Bucior, K.; Yelash, L.; Binder, K. Molecular-dynamics simulation of evaporation processes of fluid bridges confined in slitlike pores. *Phys. Rev. E* **2009**, *79*, 031604.

(19) Schapotschnikow, P.; Hommersom, B.; Vlugt, T. J. H. Adsorption and Binding of Ligands to CdSe Nanocrystals. *J. Phys. Chem. C* **2009**, *113*, 12690–12698.

(20) Sokolowski, S.; Fischer, J. Classical multicomponent fluid structure near solid substrates: Born-Green-Yvon equation versus density-functional theory. *Mol. Phys.* **1990**, *70*, 1097–1113.

(21) Sikkenk, J. H.; Indekeu, J. O.; van Leeuwen, J. M. J.; Vossnack, E. O. Molecular-dynamics simulation of wetting and drying at solid-fluid interfaces. *Phys. Rev. Lett.* **1987**, *59*, 98–101.

(22) Sikkenk, J.; Indekeu, J.; van Leeuwen, J.; Vossnack, E.; Bakker, A. Simulation of wetting and drying at solid-fluid interfaces on the Delft Molecular Dynamics Processor. *J. Stat. Phys.* **1988**, *52*, 23–44.

(23) Nijmeijer, M.; Bruin, C.; Bakker, A.; van Leeuwen, J. A visual measurement of contact angles in a molecular-dynamics simulation. *Physica A* **1989**, *160*, 166–180.

(24) Nijmeijer, M. J. P.; Bruin, C.; Bakker, A. F.; van Leeuwen, J. M. J. Wetting and drying of an inert wall by a fluid in a molecular-dynamics simulation. *Phys. Rev. A* **1990**, *42*, 6052–6059.

(25) Nijmeijer, M.; Bruin, C.; Bakker, A.; van Leeuwen, J. Molecular dynamics of the wetting and drying of a wall with a long-ranged wall-fluid interaction. *J. Phys.: Condens. Matter* **1992**, *4*, 15–31.

(26) Tang, J. Z.; Harris, J. G. Fluid wetting on molecularly rough surfaces. *J. Chem. Phys.* **1995**, *103*, 8201–8208.

(27) Blake, T. D.; Clarke, A.; De Coninck, J.; de Ruijter, M. J. Contact Angle Relaxation during Droplet Spreading: Comparison between Molecular Kinetic Theory and Molecular Dynamics. *Langmuir* **1997**, *13*, 2164–2166.

(28) Werder, T.; Walther, J. H.; Jaffe, R. L.; Halicioglu, T.; Noca, F.; Koumoutsakos, P. Molecular Dynamics Simulation of Contact Angles of Water Droplets in Carbon Nanotubes. *Nano Lett.* **2001**, *1*, 697–702.

(29) Werder, T.; Walther, J. H.; Jaffe, R. L.; Halicioglu, T.; Koumoutsakos, P. On the Water-Carbon Interaction for Use in Molecular Dynamics Simulations of Graphite and Carbon Nanotubes. *J. Phys. Chem. B* **2003**, *107*, 1345–1352.

(30) Ingebrigtsen, T.; Toxvaerd, S. Contact Angles of Lennard-Jones Liquids and Droplets on Planar Surfaces. *J. Phys. Chem. C* **2007**, *111*, 8518–8523.

(31) Grzelak, E. M.; Shen, V. K.; Errington, J. R. Molecular Simulation Study of Anisotropic Wetting. *Langmuir* **2010**, *26*, 8274–8281.

(32) Leroy, F.; Müller-Plathe, F. Solid-liquid surface free energy of Lennard-Jones liquid on smooth and rough surfaces computed by molecular dynamics using the phantom-wall method. *J. Chem. Phys.* **2010**, *133*, 044110.

(33) Rane, K. S.; Kumar, V.; Errington, J. R. Monte Carlo simulation methods for computing the wetting and drying properties of model systems. *J. Chem. Phys.* **2011**, *135*, 234102.

(34) Weijs, J. H.; Marchand, A.; Andreotti, B.; Lohse, D.; Snoeijer, J. H. Origin of line tension for a Lennard-Jones nanodroplet. *Phys. Fluids* **2011**, *23*, 022001.

(35) Shahraz, A.; Borhan, A.; Fichthorn, K. A. A Theory for the Morphological Dependence of Wetting on a Physically Patterned Solid Surface. *Langmuir* **2012**, *28*, 14227–14237.

(36) Allen, M.; Tildesley, D. *Computer Simulation of Liquids*; Clarendon: Oxford, 2009.

(37) Horsch, M.; Heitzig, M.; Dan, C.; Harting, J.; Hasse, H.; Vrabec, J. Contact Angle Dependence on the Fluid–Wall Dispersive Energy. *Langmuir* **2010**, *26*, 10913–10917.

(38) Vrabec, J.; Kedia, G. K.; Fuchs, G.; Hasse, H. Comprehensive study of the vapour-liquid coexistence of the truncated and shifted Lennard–Jones fluid including planar and spherical interface properties. *Mol. Phys.* **2006**, *104*, 1509–1527.

(39) van Meel, J. A.; Page, A. J.; Sear, R. P.; Frenkel, D. Two-step vapor-crystal nucleation close below triple point. *J. Chem. Phys.* **2008**, *129*, 204505.

(40) Hamaker, H. The London–van der Waals attraction between spherical particles. *Physica* **1937**, *4*, 1058 – 1072.

(41) Pethica, B. The contact angle equilibrium. *J. Colloid Interface Sci.* **1977**, *62*, 567 – 569.

(42) Tolman, R. C. The Effect of Droplet Size on Surface Tension. *J. Chem. Phys.* **1949**, *17*, 333–337.

(43) Engin, C.; Sandoval, L.; Urbassek, H. M. Characterization of Fe potentials with respect to the stability of the bcc and fcc phase. *Modell. Simul. Mater. Sci. Eng.* **2008**, *16*, 035005.

(44) Buchholz, M.; Bungartz, H.-J.; Vrabec, J. Software design for a highly parallel molecular dynamics simulation framework in chemical engineering. *J. Comput. Sci.* **2011**, *2*, 124 – 129.

(45) Oleinikova, A.; Brovchenko, I.; Geiger, A. Behavior of a wetting phase near a solid boundary: vapor near a weakly attractive surface. *Eur. Phys. J. B* **2006**, *52*, 507–519.

(46) Forte, E.; Haslam, A. J.; Jackson, G.; Muller, E. A. Effective coarse-grained solid-fluid potentials and their application to model adsorption of fluids on heterogeneous surfaces. *Phys. Chem. Chem. Phys.* **2014**, *16*, 19165–19180.

(47) de Gennes, P. G. Wetting: statics and dynamics. *Rev. Mod. Phys.* **1985**, *57*, 827–863.

(48) Werth, S.; Lishchuk, S. V.; Horsch, M.; Hasse, H. The influence of the liquid slab thickness on the planar vapor–liquid interfacial tension. *Physica A: Statistical Mechanics and its Applications* **2013**, *392*, 2359 – 2367.

(49) Santiso, E. E.; Herdes, C.; Müller, E. A. On the Calculation of Solid-Fluid Contact Angles from Molecular Dynamics. *Entropy* **2013**, *15*, 3734–3745.

(50) Rowlinson, J.; Widom, B. *Molecular Theory of Capillarity*; Dover: New York, 2002.

(51) Brovchenko, I.; Oleinikova, A. Universal Shape of the Fluid Density Profiles Near a Solid Boundary: LJ Vapor Near Weakly Attractive and Hard Walls. *Soft Mater.* **2012**, *10*, 106–129.

(52) Henderson, J. R.; van Swol, F. Fluctuation phenomena at a first–order phase transition. *Journal of Physics: Condensed Matter* **1990**, *2*, 4537.

(53) Monson, P. A. Contact Angles, Pore Condensation, and Hysteresis: Insights from a Simple Molecular Model. *Langmuir* **2008**, *24*, 12295–12302.

(54) Young, T. An Essay on the Cohesion of Fluids. *Phil. Trans. R. Soc. Lond.* **1805**, *95*, 65–87.

(55) Humphrey, W.; Dalke, A.; Schulten, K. VMD – Visual Molecular Dynamics. *Journal of Molecular Graphics* **1996**, *14*, 33–38.

(56) Horsch, M. T.; Miroshnichenko, S.; Vrabec, J.; Glass, C.; Niethammer, C.; Bernreuther, M.; Müller, E. A.; Jackson, G. Static and Dynamic Properties of Curved Vapour-Liquid Interfaces by Massively Parallel Molecular Dynamics Simulation. *Competence in High Performance Computing 2010*, 2010; pp 73–84.

## Supporting Information Available

The saturation densities of the curved interfaces are determined by the conditions of phase equilibrium that are stated in Eqs. (S-1) to (S-3):

$$T' = T'' \tag{S-1}$$

$$p' = p'' + \Delta p \tag{S-2}$$

$$\mu'(T, p, N) = \mu''(T, p, N), \tag{S-3}$$

where a single prime denotes the liquid phase and two primes denote the vapor phase. The chemical potential is denoted by $\mu$, and the number of fluid particles of the single fluid component by N.

For a liquid drop, the pressure difference $\Delta p$ in Eq. (S-2) is positive and is obtained from the Laplace equation,[50] Eq. (S-4):

$$\Delta p = \frac{2\gamma_{lv}}{\mathcal{R}_e}. \tag{S-4}$$

The interfacial tension data $\gamma_{lv}$ that are introduced in Eq. (S-4) are taken from the results of Vrabec et al.[38] for the LJTS fluid with a planar interface. The capillarity approximation is applied, i.e. the interfacial tension is assumed to be independent from the curvature of the interface. The radius $\mathcal{R}_e$ is obtained from Eq.(8).

At the given temperature and pressure difference, the phase equilibrium is obatained by equating the chemical potentials of the liquid and the vapor phase (see Eq. (S-3)). The chemical potential of the liquid phase is described by Eq. (S-5):

$$\mu'(T, p) = \mu_0 + \int_{p_s}^{p'} v(T, p) dp \tag{S-5}$$

where $\mu_0$ is the chemical potential at the liquid–vapor coexistence of the planar interface which serves as a refernce point. $p_s$ is the vapor pressure of the fluid with a planar interface and $p'$ is the pressure of the liquid drop according to Eq. (S-2). The molar volume $v$ is obtained by the fifth order virial isotherm of Horsch et al.[56] descirbing the saturation properties of the LJTS fluid at liquid–vapor phase coexistence.

The chemical potential of the vapor phase is described by Eq. (S-6):

$$\mu''(T,p) = \mu_0 + \int_{p_s}^{p''} v(T,p)dp \tag{S-6}$$

where $p''$ is the pressure of the vapor phase according to Eq. (S-2).

Introducing Eqs. (S-4), (S-5), and (S-6) into Eqs. (S-1) to (S-3) yields the state point at liquid–vapor coexistence and hence the molar volumes $v'$ and $v''$.

Table S.1: Contact angle of the LJTS fluid on a solid wall from the present MD simulations with a wall density of $\rho_s = 1.07\ \sigma_f^{-3}$. The correlation using Eq. (10) yields $W_0 = 1.58\ kT_c$ and $\bar{\alpha} = 0.335$.

| $\zeta$ | $kT/\epsilon_f$ | | | | |
|---|---|---|---|---|---|
| | 0.7 | 0.8 | 0.9 | 0.95 | 1.0 |
| 0.25 | 143°±4° | 154°±5° | 180°±11° | 180°±0.0° | 180°±0° |
| 0.30 | 134°±2° | 137°±2° | 157°±7° | 180°±14° | 180°±0° |
| 0.35 | 123°±2° | 130°±3° | 139°±6° | 154°±9° | 180°±0° |
| 0.40 | 114°±2° | 119°±2° | 124°±5° | 131°±5° | 145°±17° |
| 0.50 | 95°±2° | 96°±2° | 92°±2° | 100°±2° | 94°±11° |
| 0.60 | 76°±2° | 71°±2° | 68°±3° | 63°±5° | 43°±12° |
| 0.65 | 63°±2° | 60°±2° | 53°±3° | 45°±6° | 0°±0° |
| 0.75 | 35°±2° | 28°±2° | 0°±0° | 0°±0° | 0°±0° |

Table S.2: Simulation results for contact angles at a temperature of $T = 0.8\ \epsilon_f/k$ and different wall densities $\rho_s$. The parameters $W_0$ and $\bar{\alpha}$ are obtained by a correlation based on Eq. (10).

| $\rho_s/\sigma_f^{-3}$ | $\zeta$ | $\theta$ | $W_0/kT_c$ | $\bar{\alpha}/$ |
|---|---|---|---|---|
| 2.1 | 0.22 | 144°±7° | 1.82 | 0.288 |
| | 0.32 | 105°±4° | | |
| | 0.35 | 97°±2° | | |
| | 0.41 | 82°±3° | | |
| | 0.50 | 54°±5° | | |
| 4.02 | 0.20 | 139°±3° | 2.63 | 0.215 |
| | 0.25 | 117°±1° | | |
| | 0.30 | 101°±1° | | |
| | 0.35 | 83°±1° | | |
| | 0.40 | 60°±2° | | |

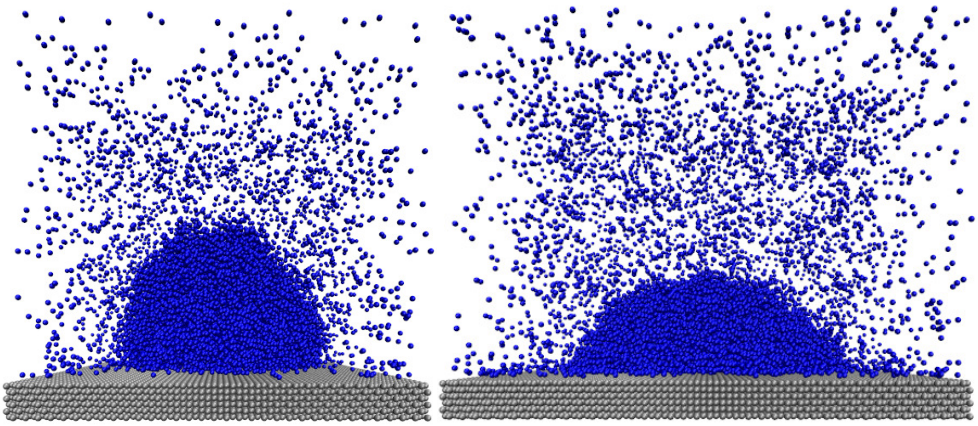

Figure S.1: Simulation snapshots taken with VMD[55] at a temperature of $T = 0.8\ \epsilon_f/k$. The reduced solid–fluid interaction energy is $\zeta = 0.25$ (left) and $\zeta = 0.65$ (right), resulting in different contact angles.

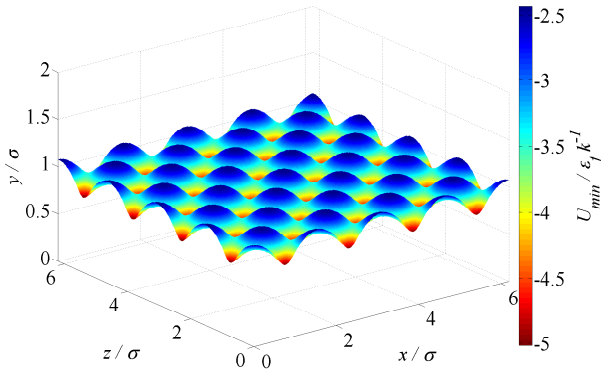


Figure S.2: Landscape of the minimal solid–fluid potential, where the normal coordinate $y$ is varied for given values of $x$ and $z$. The topography of the minimal potential is represented by the 3–dimensional surface. The color indicates the value of the solid–fluid potential energy. The structure of the lattice can be discerned.

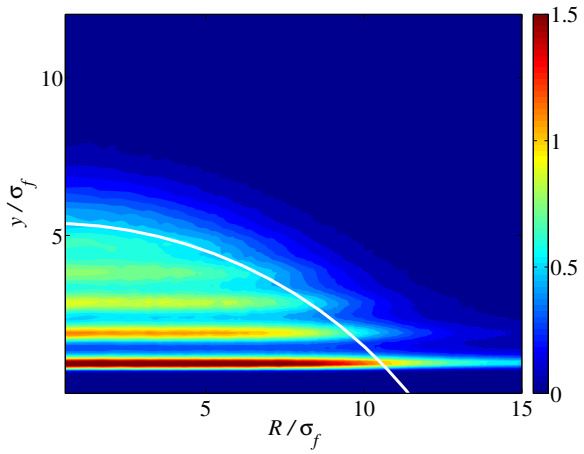


Figure S.3: Density profile of a liquid drop with a total number of 1500 fluid particles. The temperature and the reduced solid–fluid interaction energy are $T = 0.8\ \epsilon_f/k$ and $\zeta = 0.65$, respectively. The small droplet is perturbed by layering effects to which the decrease in the contact angle can be attributed. (The length scale is different from Figure 2.)

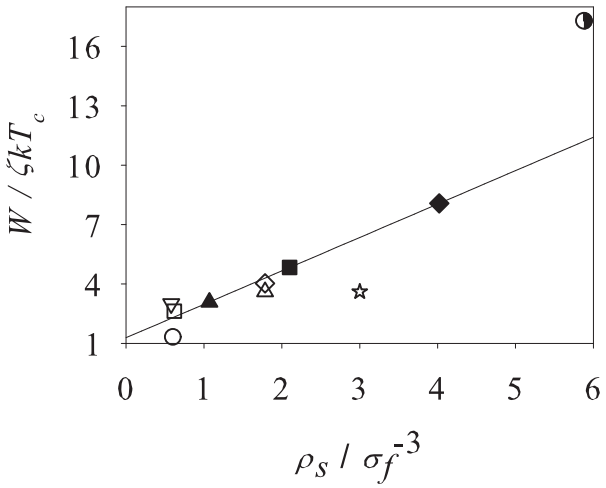


Figure S.4: Average minimum potential as a function of the solid density $\rho_s$. This work: $\rho_s = 1.07\sigma_f^{-3}$ (▲), $\rho_s = 2.10\sigma_f^{-3}$ (■), $\rho_s = 4.02\sigma_f^{-3}$ (◆). Ingebrigtsen and Toxvaerd[30] (○); Shaharaz et al.[35] (☆); Grzelak et al.[31] bcc (100) lattice (▽); Tang and Harris[26] (□); Nijmeijer et al.[24] (△); Nijmeijer et al.[25] combined model (◇); Horsch et al.[37] (◑). The line represents Eq. (5).

Table S.3: Density of the liquid phase $\rho'$ from correlation Eq. (8).

| $\zeta$ | $T = 0.7\ \epsilon_f/k$ | $T = 0.8\ \epsilon_f/k$ | $T = 0.9\ \epsilon_f/k$ | $T = 0.95\ \epsilon_f/k$ | $T = 1.0\ \epsilon_f/k$ |
|---|---|---|---|---|---|
| 0.25 | 0.7922 | 0.7379 | 0.6773 | | |
| 0.3 | 0.7901 | 0.7340 | 0.6735 | 0.6364 | 0.5857 |
| 0.35 | 0.7885 | 0.7320 | 0.6699 | 0.6367 | 0.5994 |
| 0.4 | 0.7883 | 0.7315 | 0.6649 | 0.6302 | 0.5917 |
| 0.5 | 0.7892 | 0.7317 | 0.6604 | 0.6250 | 0.5611 |
| 0.6 | 0.7915 | 0.7360 | 0.6693 | 0.6340 | 0.5567 |
| 0.65 | 0.7939 | 0.7383 | 0.6755 | 0.6887 | |
| 0.75 | 0.8083 | 0.7627 | | | |

Table S.4: Density of the vapor phase $\rho''$ from correlation Eq. (8).

| $\zeta$ | $T = 0.7\ \epsilon_f/k$ | $T = 0.8\ \epsilon_f/k$ | $T = 0.9\ \epsilon_f/k$ | $T = 0.95\ \epsilon_f/k$ | $T = 1.0\ \epsilon_f/k$ |
|---|---|---|---|---|---|
| 0.25 | 0.00824 | 0.02219 | 0.04835 | | |
| 0.3 | 0.00803 | 0.02235 | 0.05053 | 0.07260 | 0.10481 |
| 0.35 | 0.00834 | 0.02241 | 0.05012 | 0.07425 | 0.10424 |
| 0.4 | 0.00829 | 0.02231 | 0.04992 | 0.07160 | 0.10353 |
| 0.5 | 0.00852 | 0.02230 | 0.04833 | 0.06973 | 0.09742 |
| 0.6 | 0.00915 | 0.02065 | 0.04858 | 0.06559 | 0.09077 |
| 0.65 | 0.00917 | 0.02459 | 0.04521 | 0.06320 | |
| 0.75 | 0.00932 | 0.01802 | | | |

Table S.5: Equimolar radius $\mathcal{R}_e$ from correlation Eq. (8).

| $\zeta$ | $T = 0.7\ \epsilon_f/k$ | $T = 0.8\ \epsilon_f/k$ | $T = 0.9\ \epsilon_f/k$ | $T = 0.95\ \epsilon_f/k$ | $T = 1.0\ \epsilon_f/k$ |
|---|---|---|---|---|---|
| 0.25 | 16.10 | 15.90 | 14.67 | | |
| 0.3 | 16.53 | 16.15 | 14.95 | 13.65 | 12.39 |
| 0.35 | 16.89 | 16.27 | 15.18 | 13.65 | 12.69 |
| 0.4 | 17.40 | 16.85 | 15.65 | 14.24 | 12.25 |
| 0.5 | 19.46 | 18.61 | 18.51 | 15.83 | 15.78 |
| 0.6 | 22.44 | 23.95 | 22.34 | 21.33 | 21.47 |
| 0.65 | 27.16 | 26.62 | 28.66 | 27.64 | |
| 0.75 | 52.72 | 57.33 | | | |

Table S.6: Liquid–vapor interface thickness $D$ from correlation Eq. (8).

| $\zeta$ | $T = 0.7\ \epsilon_f/k$ | $T = 0.8\ \epsilon_f/k$ | $T = 0.9\ \epsilon_f/k$ | $T = 0.95\ \epsilon_f/k$ | $T = 1.0\ \epsilon_f/k$ |
|---|---|---|---|---|---|
| 0.25 | 2.338 | 3.026 | 5.478 | | |
| 0.3 | 2.318 | 2.966 | 4.163 | 5.629 | 7.822 |
| 0.35 | 2.262 | 2.963 | 4.230 | 4.904 | 6.855 |
| 0.4 | 2.258 | 2.899 | 3.862 | 4.824 | 6.983 |
| 0.5 | 2.253 | 2.858 | 3.910 | 4.613 | 6.149 |
| 0.6 | 2.233 | 2.720 | 3.900 | 4.554 | 7.035 |
| 0.65 | 2.251 | 2.762 | 3.891 | 4.024 | |
| 0.75 | 2.352 | 2.928 | | | |

Table S.7: Oscillation amplitude $A$ from correlation Eq. (8).

| $\zeta$ | $T = 0.7\ \epsilon_f/k$ | $T = 0.8\ \epsilon_f/k$ | $T = 0.9\ \epsilon_f/k$ | $T = 0.95\ \epsilon_f/k$ | $T = 1.0\ \epsilon_f/k$ |
|---|---|---|---|---|---|
| 0.25 | | | | | |
| 0.3 | 1.076 | | | | |
| 0.35 | 1.025 | | | | |
| 0.4 | 1.024 | 1.074 | 1.206 | 1.240 | 1.248 |
| 0.5 | 1.138 | 1.086 | 1.085 | 1.090 | 1.143 |
| 0.6 | 1.270 | 1.166 | 1.128 | 1.115 | 1.130 |
| 0.65 | 1.352 | 1.225 | 1.178 | 1.109 | |
| 0.75 | 1.543 | 1.386 | | | |

Table S.8: Period of the density oscillations $p$ from correlation Eq. (8).

| $\zeta$ | $T = 0.7\ \epsilon_f/k$ | $T = 0.8\ \epsilon_f/k$ | $T = 0.9\ \epsilon_f/k$ | $T = 0.95\ \epsilon_f/k$ | $T = 1.0\ \epsilon_f/k$ |
|---|---|---|---|---|---|
| 0.25 | | | | | |
| 0.3 | 0.90 | | | | |
| 0.35 | 0.91 | | | | |
| 0.4 | 0.92 | 0.90 | 0.89 | 0.91 | 0.90 |
| 0.5 | 0.93 | 0.93 | 0.90 | 0.91 | 0.89 |
| 0.6 | 0.93 | 0.95 | 0.94 | 0.92 | 0.93 |
| 0.65 | 0.93 | 0.94 | 0.94 | 0.93 | |
| 0.75 | 0.92 | 0.94 | | | |

Table S.9: Shift parameter $s$ of the density oscillation from correlation Eq. (8).

| $\zeta$ | $T = 0.7\ \epsilon_f/k$ | $T = 0.8\ \epsilon_f/k$ | $T = 0.9\ \epsilon_f/k$ | $T = 0.95\ \epsilon_f/k$ | $T = 1.0\ \epsilon_f/k$ |
|---|---|---|---|---|---|
| 0.25 | | | | | |
| 0.3 | 0.552 | | | | |
| 0.35 | 0.503 | | | | |
| 0.4 | 0.446 | 0.527 | 0.605 | 0.621 | 0.622 |
| 0.5 | 0.352 | 0.426 | 0.501 | 0.522 | 0.557 |
| 0.6 | 0.277 | 0.341 | 0.413 | 0.450 | 0.467 |
| 0.65 | 0.242 | 0.311 | 0.369 | 0.415 | |
| 0.75 | 0.187 | 0.253 | | | |

Table S.10: Damping parameter $c$ of the density oscillation from correlation Eq. (8).

| $\zeta$ | $T = 0.7\ \epsilon_f/k$ | $T = 0.8\ \epsilon_f/k$ | $T = 0.9\ \epsilon_f/k$ | $T = 0.95\ \epsilon_f/k$ | $T = 1.0\ \epsilon_f/k$ |
|---|---|---|---|---|---|
| 0.25 | | | | | |
| 0.3 | 1.570 | | | | |
| 0.35 | 1.065 | | | | |
| 0.4 | 0.855 | 1.394 | 2.655 | 3.064 | 3.026 |
| 0.5 | 0.683 | 0.927 | 1.342 | 1.415 | 1.808 |
| 0.6 | 0.629 | 0.760 | 0.962 | 1.088 | 1.208 |
| 0.65 | 0.631 | 0.743 | 0.921 | 1.051 | |
| 0.75 | 0.579 | 0.720 | | | |

Table S.11: Normal coordinate $y(\mathcal{R} = 0)$ of the centre of the droplet from correlation Eq. (8).

| $\zeta$ | $T = 0.7\ \epsilon_f/k$ | $T = 0.8\ \epsilon_f/k$ | $T = 0.9\ \epsilon_f/k$ | $T = 0.95\ \epsilon_f/k$ | $T = 1.0\ \epsilon_f/k$ |
|---|---|---|---|---|---|
| 0.25 | 13.33 | 14.87 | 18.96 | | |
| 0.3 | 11.99 | 12.39 | 14.39 | 14.54 | 19.25 |
| 0.35 | 9.94 | 11.25 | 12.10 | 13.04 | 12.81 |
| 0.4 | 7.77 | 8.78 | 9.51 | 10.00 | 11.02 |
| 0.5 | 2.21 | 2.76 | 1.43 | 3.98 | 2.13 |
| 0.6 | -4.51 | -7.33 | -7.51 | -8.73 | -13.53 |
| 0.65 | -11.59 | -12.43 | -16.31 | -19.51 | |
| 0.75 | -42.81 | -48.76 | | | |

This material is available free of charge via the Internet at http://pubs.acs.org.

# Graphical TOC Entry